

# A Hidden Active Site in the Potential Drug Target *Mycobacterium tuberculosis* dUTPase Is Accessible through Small Amplitude Protein Conformational Changes<sup>\*,§</sup>

Received for publication, May 5, 2016, and in revised form, November 4, 2016. Published, JBC Papers in Press, November 4, 2016, DOI 10.1074/jbc.M116.734012

Anna Lopata<sup>†1</sup>, Ibolya Leveles<sup>‡</sup>, Ábris Ádám Bendes<sup>‡2</sup>, Béla Viskolcz<sup>§</sup>, Beáta G. Vértessy<sup>†¶</sup>, Balázs Jójárt<sup>||</sup>, and Judit Tóth<sup>‡3</sup>

From the <sup>†</sup>Institute of Enzymology, Research Centre for Natural Sciences, Hungarian Academy of Sciences, Budapest, Hungary H1117, the <sup>§</sup>Institute of Chemistry, University of Miskolc, Miskolc, Hungary H3529, the <sup>¶</sup>Department of Applied Biotechnology, Budapest University of Technology and Economics, Budapest, Hungary H1111, and <sup>||</sup>Department of Chemical Informatics, University of Szeged, Szeged, Hungary H6725

Edited by Norma Allewell

dUTPases catalyze the hydrolysis of dUTP into dUMP and pyrophosphate to maintain the proper nucleotide pool for DNA metabolism. Recent evidence suggests that dUTPases may also represent a selective drug target in mycobacteria because of the crucial role of these enzymes in maintaining DNA integrity. Nucleotide-hydrolyzing enzymes typically harbor a buried ligand-binding pocket at interdomain or intersubunit clefts, facilitating proper solvent shielding for the catalyzed reaction. The mechanism by which substrate binds this hidden pocket and product is released in dUTPases is unresolved because of conflicting crystallographic and spectroscopic data. We sought to resolve this conflict by using a combination of random acceleration molecular dynamics (RAMD) methodology and structural and biochemical methods to study the dUTPase from *Mycobacterium tuberculosis*. In particular, the RAMD approach used in this study provided invaluable insights into the nucleotide dissociation process that reconciles all previous experimental observations. Specifically, our data suggest that nucleotide binding takes place as a small stretch of amino acids transiently slides away and partially uncovers the active site. The *in silico* data further revealed a new dUTPase conformation on the pathway to a relatively open active site. To probe this model, we

developed the Trp<sup>21</sup> reporter and collected crystallographic, spectroscopic, and kinetic data that confirmed the interaction of Trp<sup>21</sup> with the active site shielding C-terminal arm, suggesting that the RAMD method is effective. In summary, our computational simulations and spectroscopic results support the idea that small loop movements in dUTPase allow the shuttling of the nucleotides between the binding pocket and the solvent.

Commonly, nucleotide-hydrolyzing enzymes harbor a binding pocket for their cognate ligand at interdomain or intersubunit clefts. This arrangement facilitates proper solvent shielding for the catalyzed reaction. Many well described enzymes bind nucleotides in a relatively open (e.g. DNA and RNA helicases, molecular motors, and small G-proteins) or completely open (ATP-dependent DNA ligases) binding pocket. Conformational changes associated with nucleotide binding result in the closure of the active site, enabling the subsequent reaction steps (1–5). The conformational change of the enzyme upon nucleotide binding can be understood by comparing the available apo and ligand-containing crystal structures. However, using single molecule optical spectroscopy in addition to the static structural data, the nucleotide binding pocket of DNA polymerase I was shown to exhibit dynamic open-closed equilibrium in the binary complex with DNA that is shifted toward the closed conformation upon dNTP binding (6). In such a case, the ligand may bind to a pocket that appears relatively closed on a millisecond-second time scale.

Homotrimeric dUTPases have three equivalent active sites in the clefts constituted by two neighboring subunits (Fig. 1) (7, 8). The C-terminal arm of the third subunit folds over the active site and shields the substrate from the solvent (Fig. 1A). This segment of the polypeptide is only visible in protein crystals that contain substrate analogues. In the apo state, the C-terminal arm is undefined in the crystal structures of dUTPases from widely different species (9–11). This observation has been interpreted as an open-closed transition of the C-terminal arm and the active site. The steady-state conformational states of the C-terminal arm were probed by a fluorescent sensor (Trp<sup>158</sup> in human dUTPase). The measured solvent accessibility of this sensor in various nucleotide-bound states suggested that the

<sup>\*</sup>This work was supported by National Institutes of Health Grant 1R01TW008130; National Research, Development and Innovation Office Hungarian Scientific Research Fund Grants OTKA K109486, K115993, and K119493; the Hungarian Academy of Sciences MedInProt Program; International Centre for Genetic Engineering and Biotechnology (ICGEB) Research Grant CRP/HUN14-01; and Hungarian Scientific Research Funds. The authors declare that they have no conflicts of interest with the contents of this article. The content is solely the responsibility of the authors and does not necessarily represent the official views of the National Institutes of Health.

<sup>§</sup>This article contains supplemental Movies S1–S5.

<sup>1</sup>Present address: Laboratory of Molecular Physiology, NHLBI, National Institutes of Health, Bethesda, MD 20892; and School of Molecular and Cellular Biology, Faculty of Biological Sciences, University of Leeds, Leeds, UK, LS2 9JT.

<sup>2</sup>Present address: Faculty of Biochemistry and Molecular Medicine, University of Oulu, Oulu, Finland, 90014; and Biocenter Oulu, University of Oulu, Oulu, Finland, 90014.

<sup>3</sup>Recipient of the János Bolyai Research Scholarship of the Hungarian Academy of Sciences. To whom correspondence should be addressed: Institute of Enzymology, Research Centre for Natural Sciences, Hungarian Academy of Sciences, Magyar tudósok körútja 2, Budapest, Hungary, H1117. Tel.: 36-1-3826707; Fax: 36-1-4631401; E-mail: toth.judit@ttk.mta.hu.

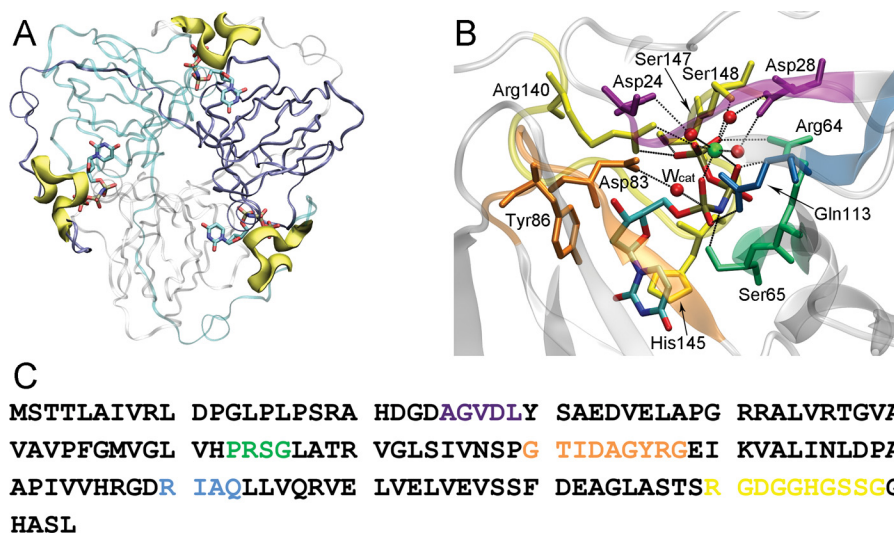


**FIGURE 1. Three-dimensional structure and conserved motifs of the *M. tuberculosis* dUTPase.** *A*, three-dimensional structure of the *M. tuberculosis* dUTPase enzyme complexed with dUPNPP (PDB code 2PY4 (33)). The subunits are shown as white, cyan, and blue ribbons, whereas the fifth conserved motif located on the C-terminal arm is highlighted as thick yellow ribbon in all subunits. *B*, three-dimensional structure of the active site of *M. tuberculosis* dUTPase enzyme complexed with dUPNPP (PDB code 2PY4 (33)). The protein backbone is shown as white ribbon, and the conserved motifs are highlighted with stick representation of different colors (violet, green, orange, blue, and yellow for first, second, third, fourth, and fifth conserved motif, respectively). dUTP is visualized by atomic colored stick representation.  $Mg^{2+}$  ion, the water molecules of the  $Mg^{2+}$  ion coordination sphere, and the catalytic water molecule are shown as green and red spheres, respectively. *C*, amino acid sequence of the *M. tuberculosis* dUTPase. The conserved motifs are color-coded according to *B*.

arm resides in a relatively closed conformation during the large fraction of the reaction cycle time (12). A presumed open-closed conformational transition upon ligand binding could not be observed. Because of the seeming contradictory evidence between the crystallographic and fluorescence spectroscopy data, we could not establish a comprehensive model of substrate binding or product release. To fill this gap, we implemented the random acceleration molecular dynamics (RAMD)<sup>4</sup> method for its ability to gain high resolution information on the enzyme-nucleotide interaction. Under physiological conditions, ligand binding and dissociation usually takes place on a microsecond-millisecond time scale and requires several microsecond long molecular dynamics simulation for accurate modeling (13–16). Therefore, in case of buried active sites, guided or biased molecular dynamics simulations such as steered molecular dynamics (17, 18), RAMD (19), and metadynamics (20, 21) are preferably used to accelerate the process of ligand binding or dissociation. The RAMD method (19) applies an artificial random oriented force that acts on the ligand and accelerates the dissociation process, offering a reasonable time scale for computational simulations. Because of the reduced simulation time scale and the randomly oriented force, a larger sample size of ligand dissociation pathways are explored at atomic resolution. Considering that ligand binding is a reversible process, this method can be used to explore substrate dissociation and binding pathways as well (19). The RAMD method has been successfully employed to study ligand dissociation paths in cytochrome P450 (19), rhodopsin (22), haloalkane dehalogenase (23), histone deacetylase (24), heme oxygenase (25), thyroid hormone receptor (26),

P-glycoprotein (27), and B-Raf kinase (28), among many others.

High resolution crystal structures (10, 29–35), a detailed kinetic mechanism (12, 36, 37) and additional regulatory functions (38–40) have already been revealed for dUTPases in a wide variety of species. Previously, we have investigated the detailed mechanism of substrate binding, hydrolysis, and product release in dUTPase using a combination of structural and transient kinetics methods (12, 41). These results obtained from crystal structures and from spectroscopic measurements on the millisecond time scale movements did not allow insights into the possible substrate binding pathways to the hidden active site of dUTPase. This process may have pharmacological significance because we have recently shown that the dUTPase enzyme may be a selective drug target in mycobacteria (42). This enzyme plays a crucial role in DNA integrity by catalyzing the hydrolysis of dUTP into dUMP and pyrophosphate, producing the precursor for dTTP biosynthesis. At the same time, the dUTPase reaction is also responsible for balancing a low intracellular dUTP:dTTP ratio required in most organisms to avoid DNA uracilation that may have serious consequences (8, 43).

In this study, we determine the putative ligand shuttling pathway of dUTP between the solvent and the active site of the *Mycobacterium tuberculosis* dUTPase using RAMD simulations in combination with experimental methods including X-ray crystallography, fast kinetics, ligand binding, and solvent accessibility experiments. The results suggested that active site residues are predominately in the closed conformation over the entire reaction cycle and during the nucleotide binding process. We observe a small stretch of amino acids that slides transiently away with small amplitude movements to partially uncover the active site. In addition,

<sup>4</sup> The abbreviations used are: RAMD, random acceleration molecular dynamics; PDB, Protein Data Bank; RMSD, root mean square deviation; dUPNPP, 2'-deoxyuridine 5'- $\alpha,\beta$ -imido-triphosphate; NATA, *N*-acetyl-L-tryptophanamide.

# Nucleotide Dissociation from a Hidden Active Site

this is the first study that demonstrates direct experimental validation of the powerful RAMD method.

## Results

*RAMD Simulations Reveal the High Spatiotemporal Resolution Movements of the Active Site upon Substrate Unbinding*—Of 72 individual RAMD simulations performed, 55 led to productive dissociation of the ligand from the active site. In the remaining 17 runs, the ligand did not exit the active site during the entire 300-ps length of the simulations. A representative of unproductive simulations can be seen in Fig. 2.

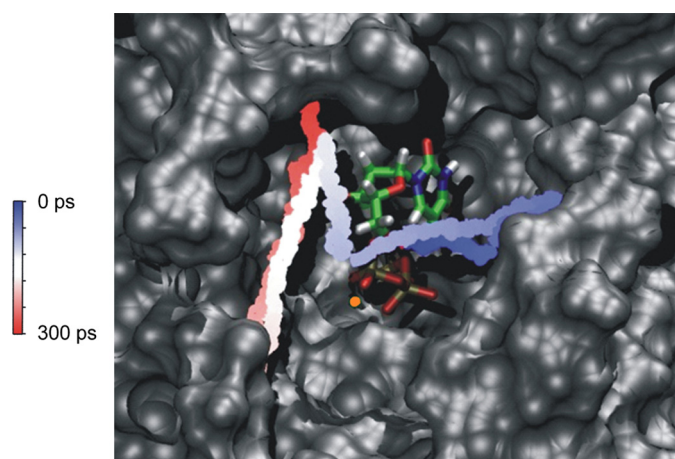


FIGURE 2. **A representative of the 17 unproductive RAMD runs.** The enzyme can be seen with gray surface representation. For clarity, the C-terminal arm is omitted from this picture. dUTP is visualized as atomic coloring stick model, and  $Mg^{2+}$  is an orange sphere. The path of the center of mass of the dUTP- $Mg^{2+}$  complex is visualized as a blue, white, and red line.

Based on the order of dissociation of the substrate from the various interaction points within the protein listed below, the 55 productive RAMD runs could be classified into five major unbinding pathways A–E (Fig. 3). The difference between these paths can be best appreciated visually by watching [supplemental Movies S1–S5](#). To understand the classification criteria in the text format analysis in Table 1, it is crucial to describe the interactions of the substrate within the active site. The first conserved motif (violet in Fig. 1, B and C) coordinates the  $Mg^{2+}$  of the physiological substrate- $Mg^{2+}$  complex through water molecules. The second and fourth motifs (green and blue, respectively in Fig. 1, B and C) coordinate the phosphate chain of the substrate, whereas the third motif (orange in Fig. 1, B and C) maintains interactions with the uracil and deoxyribose moieties of the nucleotide (35). The fifth motif (yellow in Fig. 1, B and C) located on the C terminus coordinates the  $\gamma$ -phosphate and the uracil ring of the substrate and is responsible for diphosphate/triphosphate ligand discrimination mainly by promoting hydrolysis of the triphosphate nucleotide (41). In agreement with this, it has been shown in a wide variety of dUTPases that the enzymatic activity of C-terminally truncated mutants is drastically lower (practically 0) than that of the WT (11, 34, 37, 41, 44, 45).

The structural element in the focus of the present study is the fifth motif as it shields the nucleotide binding cavity and restricts nucleotide shuttling. Fig. 4 highlights the position of this motif relative to the observed exit routes and also shows its overall conformational change between the initial and final time points of the RAMD runs. In pathway A, the N-terminal part of the C-terminal arm transiently moves away from the enzyme core as the substrate leaves the active site, whereas the

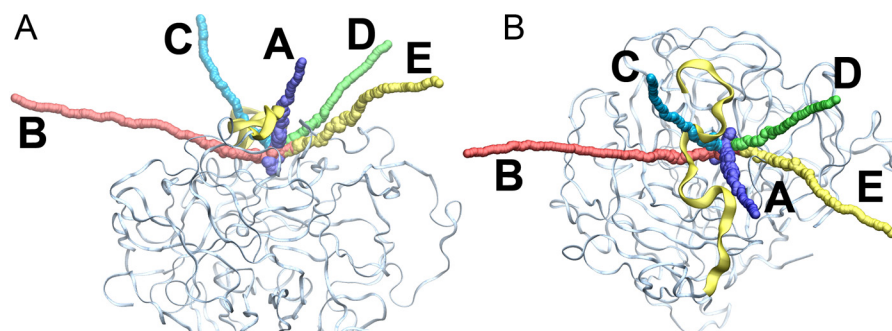


FIGURE 3. **Exit routes of five representative simulations from the five major ligand unbinding pathways.** A, the enzyme is shown with light blue ribbon model, and the C-terminal arm is highlighted as flat yellow ribbon. The curves, representing the five major pathways, are the sphere models of the center of mass of the dUTP- $Mg^{2+}$  complex during the course of simulations. B, the same structures upon rotating the protein by 90°.

TABLE 1

## Analysis of the five ligand binding pathways

In the RMSD calculation, 305 atoms (residues 130–154) were superposed.

Pathway name	A	B	C	D	E
Number of runs	6	6	18	19	6
Substrate dissociation from indicated protein segments in the order of interaction break-up (M stands for conserved motif)	M4 M2 M1 M3 M5	M1 M4 M3 M2 Leu <sup>44</sup> Lys <sup>91</sup> M5	M3 M1 M2 M4 M5	M3 M2 M1 M4 M5	M3 M2 M4 Phe <sup>55</sup> Val <sup>119</sup> –Glu <sup>123</sup> M1 M5
Maintenance of octahedral coordination between $Mg^{2+}$ and the phosphate oxygens of dUTP	No	Yes	No	Yes	Yes
RMSD of the C-terminal arm (Å)	5.6 ± 1.4	3.4 ± 0.5	6.7 ± 2.2	4.6 ± 0.8	6.3 ± 1.3



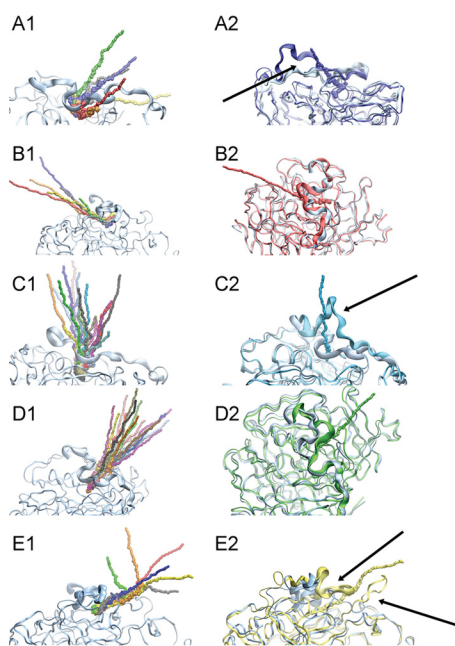


FIGURE 4. Initial structures and exit routes of the dUTP-Mg<sup>2+</sup> complex of all simulations (panels A1–E1) and end point protein structures of representative runs (panels A2–E2) from the five major pathways (A–E). The enzyme is shown as light blue ribbon model, and the C-terminal arm is highlighted as flat ribbon. The curves representing the runs are the sphere models of the center of the dUTP-Mg<sup>2+</sup> complex during the course of simulations. Arrows indicate the notable conformational changes between the start and end point structures.

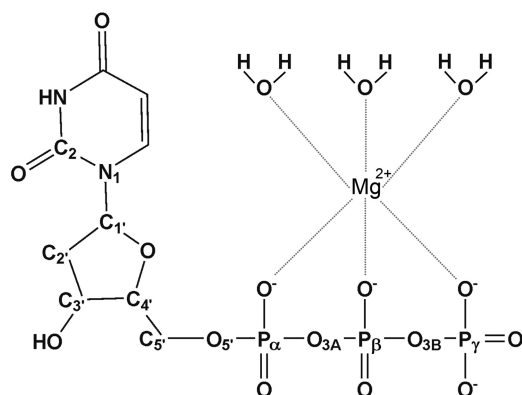


FIGURE 5. Schematic representation of the dUTP-Mg<sup>2+</sup> complex. The coordination sphere of the Mg<sup>2+</sup> ion is constituted from the phosphate chain of dUTP and three water molecules.

rest of the C-terminal arm keeps its position (Fig. 4A and [supplemental Movie S1](#)). In pathway C, partial unfolding of the C-terminal arm can be observed, whereas all intermolecular contacts are broken between the C-terminal arm and the protein core (Fig. 4C and [supplemental Movie S3](#)). In contrast, the C-terminal arm moves on the surface of the protein without losing its interactions with the rest of the protein in pathways B, D, and E (Fig. 4, B, D, and E, and [supplemental Movies S2, S4, and S5](#)). In three of the runs (shown in green, orange, and gray in Fig. 4E), the route of ligand exit changes its direction after its initial progress, which is due to a steric clash with the first conserved motif forcing the ligand to exit at different directions.

Another subtle difference that was observed during the analysis of the RAMD runs was that in pathways A and C, but not in pathways B, D, or E, the coordination geometry between Mg<sup>2+</sup>

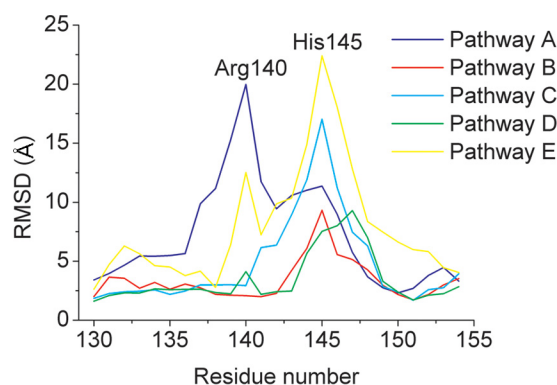


FIGURE 6. Maximal RMSD values of single amino acids in the C-terminal arm during the five representative RAMD runs.

and the phosphate chain of dUTP (Fig. 5) becomes distorted as the ligand exits the active site (Table 1). This distortion coincides with a larger conformational change of the C-terminal arm as also reflected by the root mean square deviation (RMSD) for the C-terminal arm between the initial and final conformations (Table 1).

Importantly, the C-terminal arm remains close to the enzyme core in each RAMD simulation as opposed to opening up completely and exposing the active site to the solvent ([supplemental Movies S1–S5](#)). A quantitative analysis of the displacement of amino acids within the C-terminal arm can be viewed in Fig. 6. The small RMSD values characteristic to amino acids 130–135 and 150–155 indicate that the proximal and distal regions of the arm stay in contact with the enzyme core. The fifth conserved motif is situated in between these sequences and takes active part in the ligand exit process as reported by the elevated RMSD values. His<sup>145</sup> acts as the aromatic lid over the active site present in all dUTPases by engaging in a  $\pi$ - $\pi$  stacking interaction with uracil (Fig. 1B) (35, 46). This interaction was earlier exploited to study the enzymatic cycle as it reports on ligand binding and product unbinding using various spectroscopic methods (12). The high RMSD values of His<sup>145</sup> explain the observed spectroscopic changes and reinforce the importance of  $\pi$ - $\pi$  stacking interactions in directing ligand exit (47). Arg<sup>140</sup>, responsible for  $\gamma$ -phosphate coordination, also displays relatively high RMSD values in pathways A and E. This phenomenon will be discussed in the subsequent sections.

These RAMD results provide the first body of evidence that reconciles all the previous ensemble spectroscopic measurements and crystallographic data concerning the movements and role of the C-terminal arm during substrate binding. Upon substrate binding or product release, the nucleotide moves through small and transient spaces available as a stretch of the C-terminal polypeptide chain moves away from the shielding position. Such a mechanism involves relatively small conformational changes (12) of a yet dynamic C-terminal arm (37, 48) and a relatively closed active site even without bound substrate (12).

*New Substrate-dependent Interaction Point Detected in the RAMD Runs*—During detailed analysis of the pathways, some less conserved residues in the neighborhood of the conserved motifs appeared to take active part in the substrate unbinding

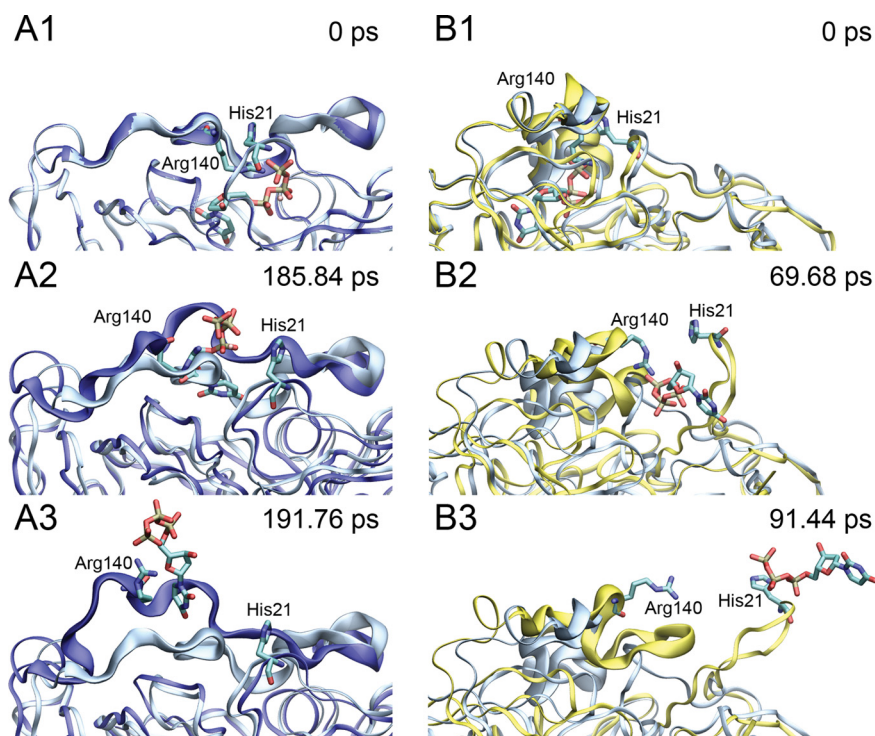


FIGURE 7. Snapshots from pathways A and E showing the His<sup>21</sup>–Arg<sup>140</sup> interaction. The initial enzyme structure is shown as light blue ribbon model, whereas the actual structure during the course of the simulation is shown as a blue and yellow ribbon model for pathways A (panels A1–A3) and E (panels B1–B3), respectively. The C-terminal arm is highlighted as thick ribbon in all cases. The dUTP-Mg<sup>2+</sup> complex and the His<sup>21</sup> and Arg<sup>140</sup> residues are visualized as stick models with atomic coloring, and the hydrogen atoms are omitted for clarity.

TABLE 2

Data collection and refinement statistics of PDB code 4GKY

Space group	P 6 <sub>3</sub>
Unit cell	
<i>a</i> , <i>b</i> , <i>c</i> (Å)	54.94, 54.94, 83.86
$\alpha$ , $\beta$ , $\gamma$ (°)	90, 90, 120
Resolution (Å)	27.95–1.50 (1.58–1.50) <sup>a</sup>
Total no. of reflections	173,193
No. of unique reflections	23,022
Redundancy	7.5 (4.8)
Completeness (%)	100 (100)
$\langle I \rangle / \langle \sigma(I) \rangle$	11.8 (2.1)
<i>R</i> <sub>meas</sub> (%) <sup>b</sup>	0.085 (0.578)
Refinement	
No. of protein atoms	1216
Ligand atoms/water/Mg <sup>2+</sup> ions	28/156/1
<i>R</i> <sub>cryst</sub> / <i>R</i> <sub>free</sub> (%) <sup>c,d</sup>	12.35/15.62
Overall B-factors (Å <sup>2</sup> ) <sup>e</sup>	25.862/21.482/27.401/22.047
Deviations from ideal stereochemistry	
RMSD bonds (Å)	0.015
RMSD angles (°)	1.555
Ramachandran plot analysis <sup>f</sup>	
Most favored (%)	99.30
Additionally allowed (%)	0.70
Disallowed (%)	0.00

<sup>a</sup> The values in parentheses are for the highest resolution shell.

<sup>b</sup>  $R_{\text{meas}} = \sum [n/(n-1)]^{1/2} (|I_i - \langle I \rangle|) / \sum \langle I \rangle$ , where the sum is calculated over all observations of a measured reflection (*I*<sub>i</sub>), and  $\langle I \rangle$  is the mean intensity of all the measured observations (*I*<sub>i</sub>).

<sup>c</sup>  $R_{\text{cryst}} = \sum (|F_{\text{obs}} - F_{\text{calc}}|) / \sum (F_{\text{obs}})$ , where *F*<sub>obs</sub> is the observed structure factor amplitude, and *F*<sub>calc</sub> is that calculated from the model.

<sup>d</sup> *R*<sub>free</sub> is equivalent to *R*<sub>cryst</sub> but where 5% of the measured reflections have been excluded from refinement in thin shells and set aside for cross-validation purposes.

<sup>e</sup> Average *B* values for all atoms/ligand atoms/water/Mg<sup>2+</sup> ions.

<sup>f</sup> Ramachandran plot analysis was from MolProbity.

process. Particularly, a yet undescribed stacking interaction between the imidazole ring of His<sup>21</sup> (N-terminal of the first conserved motif) and the guanidino group of Arg<sup>140</sup> (fifth conserved motif) residues displayed characteristic changes. This

interaction in pathways A and E seems to break up as the ligand exits the active site (Fig. 7 and supplemental Movies S1 and S5), also explaining the large displacement of Arg<sup>140</sup> indicated in Fig. 6. In the other three pathways, this interaction persists during the entire simulation. We found this phenomenon interesting because it directly involves the opening of the active site and the anchoring of the C-terminal arm (Arg<sup>140</sup>) to the enzyme core (His<sup>21</sup>). We carried out the further detailed biochemical and structural biology experiments to validate this *in silico* observation and to learn more about the substrate binding process.

**Implementation of a Reporter to Study the His<sup>21</sup>–Arg<sup>140</sup> Interaction**—To continuously monitor the interaction between His<sup>21</sup> and Arg<sup>140</sup> during the reaction cycle, we introduced a single Trp fluorescent sensor into position 21. We already had experience with His to Trp changes in this protein that left the protein fold and activity unaffected and provided useful signals (33, 42, 49). Position 21 is conserved in the bacterial phylum Actinobacteria. Tyr may replace His in some sequences (Atopobium, Olsonella, and Actinoplanes), which also suggests that the aromatic nature of the amino acid in this position is important. The H21W point mutant *M. tuberculosis* dUTPase was thus generated to study the dynamic behavior of the interaction between the protein core and the C-terminal arm of the protein.

**Crystal Structure of the H21W Mutant**—The crystal structure of the H21W mutant has been solved to 1.5 Å resolution and deposited to the PDB database under code 4GKY (for crystallographic data see Table 2). The global structure of the mutant enzyme is highly similar to the WT (PDB code 2PY4



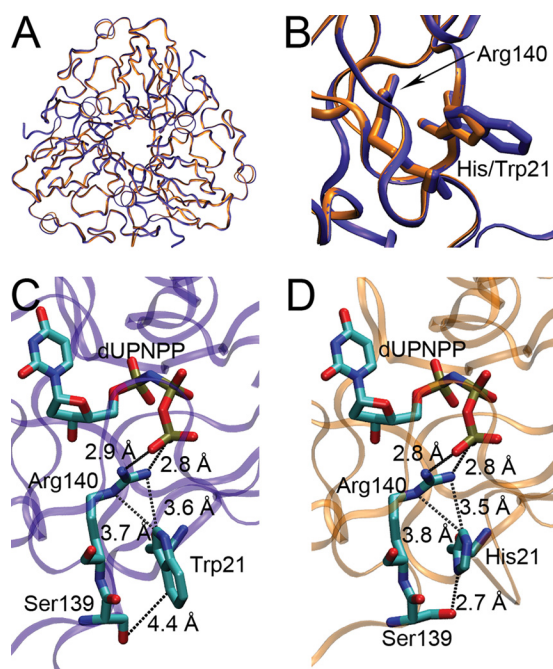


FIGURE 8. **Crystal structure of the H21W mutant.** A, superimposition of the WT *M. tuberculosis* dUTPase (PDB code 2PY4 (33), orange) and the H21W mutant (PDB code 4GCV, violet). The proteins are visualized as colored ribbon model, and dUPNPP can be seen as atomic colored sticks. The global structures of the two proteins are highly similar, which is supported by the 0.2 Å RMSD of the protein backbone atoms. B, enlarged view of A, where the side chains of the mutated residues are shown as stick models. The indole ring of the Trp residue and the imidazole ring of the His residue are in the same position. C and D, possible interacting points of the Trp<sup>21</sup> residue (C) or the His<sup>21</sup> residue (D) are Ser<sup>139</sup> and Arg<sup>140</sup> from the crystal structure of the H21W mutant (C) or the WT *M. tuberculosis* dUTPase (D). Arg<sup>140</sup> is coordinating the  $\gamma$ -phosphate oxygen of the substrate. The protein backbone is shown as violet (C) or orange (D) ribbon model, and the residues and the non-hydrolyzable substrate analogue dUPNPP can be seen as atomic colored sticks.

(33)), which is clearly demonstrated by the 0.2 Å RMSD of the protein backbone atoms (Fig. 8A). It should be mentioned that parts of the flexible termini of the structure are affected by slight model bias and are flagged as real space  $R$  value  $Z$  score outliers. This, however, does not affect the accurate interpretation of the protein core and the discussed residues of interest. Thus, the active site can be considered as equivalent to that of the WT. The RMSD of the non-hydrolyzable substrate analogue dUPNPP-Mg<sup>2+</sup> complexes in the reference and new structure is 0.1 Å. The mutant Trp side chain is in the same position as the His side chain in the WT (Fig. 8B), despite the fact that the indole ring of the Trp residue is larger and more hydrophobic than the imidazole ring of the His. The indole ring establishes similar interactions with the backbone atoms of Ser<sup>139</sup> and Arg<sup>140</sup> and with the side chain of Arg<sup>140</sup> (Fig. 8C) to those of the imidazole ring (Fig. 8D). The hydrogen bond with the side chain of Ser<sup>139</sup> vanished upon the substitution. Arg<sup>140</sup> is the first residue of the fifth conserved motif. It has a crucial role in the coordination of the  $\gamma$ -phosphate of the substrate by a bifurcated hydrogen bond (10) and hence in the enzymatic catalysis (41, 50). These structural similarities suggest a WT behavior for the H21W mutant similar to a previously described H145W mutant, where the mutated aromatic residue stacks against the uracil ring of the substrate establishing a  $\pi$ - $\pi$  stacking interaction (35).

TABLE 3

Kinetic and thermodynamic parameters measured for the H145W and H12W *M. tuberculosis* dUTPase mutants

$k_{\text{cat}}$ , catalytic rate constant obtained from steady-state measurements;  $k_{1\text{ on}}$ , second order dUTP binding rate constant obtained from stopped flow measurements;  $k_{1\text{ off}}$ , dUTP dissociation rate constant obtained from stopped flow measurements;  $k_{2\text{ obs}}$ , observed isomerization rate constant for dUTP binding;  $K_{d,\text{dUPNPP}}$ , dissociation constant for the enzyme-dUPNPP complex obtained from equilibrium fluorescence titration;  $K_{d,\text{dUDP}}$ , dissociation constant for the enzyme-dUDP complex obtained from equilibrium circular dichroism titration.

	H145W	H21W
$k_{\text{cat}}$ (s <sup>-1</sup> )	3.1 ± 0.06 (35)	2.9 ± 0.3
$k_{1\text{ on}}$ (s <sup>-1</sup> μM <sup>-1</sup> )	29.2 ± 1.7	8.0 ± 0.7
$k_{1\text{ off}}$ (s <sup>-1</sup> )	104 ± 20	165 ± 13
$k_{2\text{ obs}}$ (s <sup>-1</sup> )	13.2 ± 2.4	36.2 ± 12.4
$K_{d,\text{dUPNPP}}$ (μM)	0.32 ± 0.1	2.9 ± 0.6
$K_{d,\text{dUDP}}$ (μM)	22.5 ± 9.4	1.9 ± 1.0

**Enzymatic Mechanism Probed by Transient Kinetics**—The  $k_{\text{cat}}$  of the H21W mutant was measured to be 2.9 s<sup>-1</sup> (Table 3) which is comparable with that of the WT (3.1 s<sup>-1</sup> according to Pecsí *et al.* (35)). Next, we assayed whether the fluorescence of the Trp<sup>21</sup> residue reports any events of the reaction cycle. Surprisingly, the H21W mutant displays similar fluorescent signal change during the enzymatic cycle as previously reported for the H145W active site Trp mutant (Fig. 9A) (35, 49). In the H21W mutant, however, the Trp residue is outside of the active site, presumably far from the substrate during the chemical reaction. It is only connected to the active site through the interaction with Arg<sup>140</sup> pointed out in our RAMD runs. This suggests that the movements of the C-terminal arm during the reaction are efficiently transmitted to the Trp<sup>21</sup> residue. As a result, the fluorescence intensity of the Trp<sup>21</sup> residue decreases upon substrate binding and remains quenched in the steady-state hydrolysis phase to recover upon products dissociation (Fig. 9A).

Using the large fluorescent signal, we recorded time courses in substoichiometric dUTP concentrations in the stopped flow apparatus to obtain the true single turnover rate constant ( $k_{\text{sto}}$ ) of the dUTPase reaction (Fig. 9A). The exponential fit to the fluorescence recovery phase yielded  $k_{\text{sto}} = 3.1$  s<sup>-1</sup>. The observation that  $k_{\text{cat}}$  equals  $k_{\text{sto}}$  with a fluorescent reaction profile similar to that of the H145W dUTPase implies the same enzymatic mechanism in which dUTP hydrolysis is rate-limiting (12).

The kinetics of dUTP binding was also measured using stopped flow (Fig. 9B). For comparison, the yet undescribed substrate binding kinetics of H145W was measured as well (Fig. 9C) (our previous kinetic investigation (12) was carried out using the human enzyme). The observed ligand binding rate constants are plotted against the ligand concentration and fitted with linear functions to obtain the microscopic association and dissociation rate constants ( $k_{\text{on}}$  and  $k_{\text{off}}$ , respectively; Fig. 9, D and E, and Table 3). Compared with the human enzyme, the *M. tuberculosis* H145W enzyme displays similarly high  $k_{\text{off}}$  value and somewhat lower  $k_{\text{on}}$  value. Rate constants of the H21W mutant are in the same range as those for the H145W; however, there is a 3.5-fold decrease in the  $k_{\text{on}}$  value and a 50% increase in the  $k_{\text{off}}$  value. The apparent dissociation constants of the enzyme-dUTP complexes could not be determined from the amplitudes of the fluorescence change caused by saturating conditions. In view of the structural similarity between the two

## Nucleotide Dissociation from a Hidden Active Site

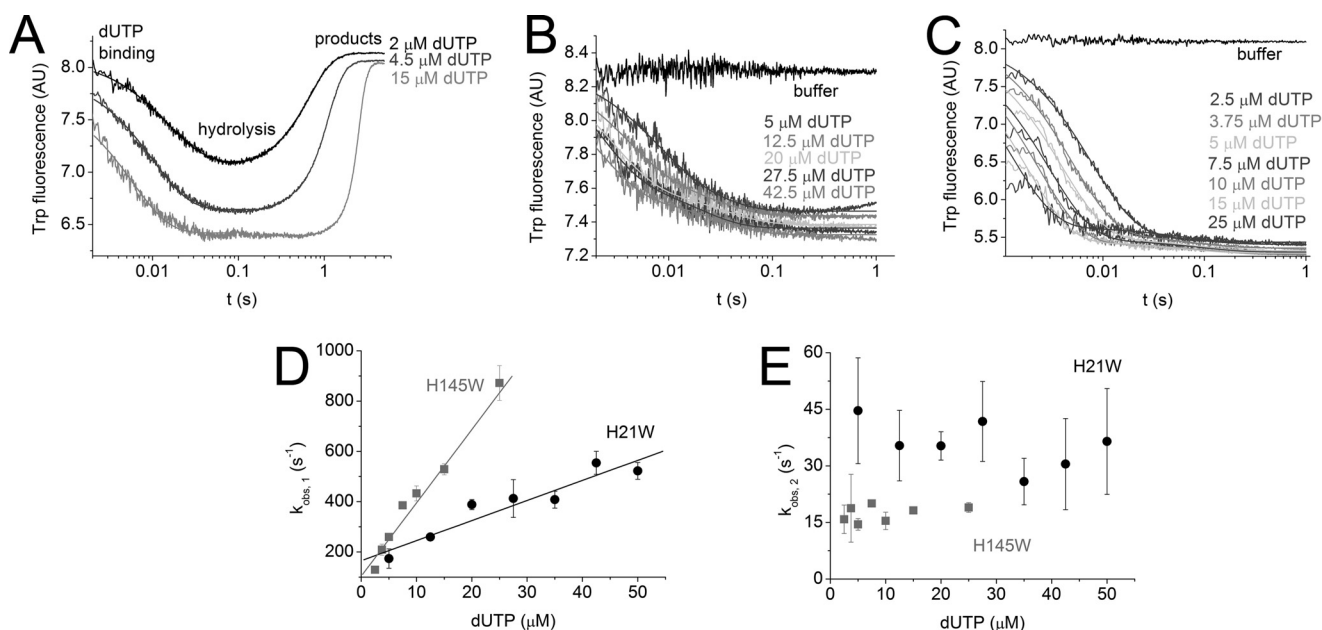


**FIGURE 9. Fast kinetics of the H21W and H145W mutants.** The latter was described earlier to display WT behavior (35). *A*, the fluorescence time courses of the H21W mutant hydrolyzing sub- and superstoichiometric amounts of substrate show similar progression to those reported for the H145W mutant. 3  $\mu\text{M}$  enzyme was mixed with various concentrations of dUTP (post-mix concentrations). Triple exponential function was fitted to the single turnover curve obtained for the lowest, substoichiometric dUTP concentration which yielded  $3.1\text{ s}^{-1}$  for the third phase ( $k_{1,\text{obs}} = 69\text{ s}^{-1}$ ,  $k_{2,\text{obs}} = 3.6\text{ s}^{-1}$ ). In earlier works, this rate constant was identified as the single turnover rate constant ( $k_{\text{STO}}$ ) (12). *B* and *C*, dUTP binding to the H21W (*B*) or to the H145W (*C*) mutant. 1  $\mu\text{M}$  enzyme was mixed with buffer or with various concentrations of dUTP in pseudo first order conditions. Double exponential function was fitted to the data. *D*, concentration dependence of the observed catalytic rate constants of the fast phase of dUTP binding ( $k_{\text{obs},1}$ ). *E*, concentration dependence of the observed catalytic rate constants of the slow phase of dUTP binding ( $k_{\text{obs},2}$ ). This phase seems to be independent of the substrate concentration in agreement with previous data.

enzymes (Fig. 8), it was not expected that the ligand binding process would be much slower when a Trp residue is present instead of a His in position 21. This change, however, further proves that this residue is involved in the ligand binding pathway.

**Ligand Binding**—To reveal more mechanistic details of the involvement of residue 21 in the ligand binding/dissociation pathways, we carried out comparative fluorescence and circular dichroism studies. The fluorescent spectra of the apo H21W mutant enzyme and its complexes with dUMP, dUDP, and the dUTP-mimicking, practically non-hydrolyzable dUPNPP were recorded (Fig. 10A). The relative fluorescence quench induced by these ligands differs considerably from that observed previously in the H145W mutant (Fig. 10B). Only dUPNPP induced a significant fluorescence intensity decrease, whereas the dUDP and dUMP complexes of the H21W mutant remained fluorescently silent. In contrast, all ligand-enzyme complexes of H145W show a decrease in fluorescence intensity (49) according to the extent of C-terminal arm rigidity, which stabilizes the stacking interaction between the indole ring of Trp and uracil (12). The Trp incorporated in the H21W mutant thus only reports the binding of the triphosphate nucleotides. This phenomenon is consistent with the RAMD results, suggesting that the Trp<sup>21</sup> residue is in interaction with Arg<sup>140</sup> responsible for coordinating the  $\gamma$ -phosphate of the ligand exclusively (Fig. 8C). The dissociation constant of the enzyme-dUPNPP complex was determined using fluorescence intensity titrations and was found to be 1 order of magnitude larger than that of the H145W-dUPNPP complex (Fig. 10C).

Binding of dUDP could not be measured using fluorescent titration in a lack of a detectable signal (Fig. 10A). However, to

ensure that dUDP indeed binds to the H21W mutant, circular dichroism titration measurements were performed. Determination of the  $K_d$  of the enzyme-dUDP complex using this method is only possible with relatively high error because the concentrations applied in the measurements are necessarily far above the  $K_d$ . Nevertheless, it is clear from the data that the H21W mutant binds dUDP significantly tighter than the H145W ( $p = 0.046$ ) (Fig. 10D).

The results of the nucleoside mono-, di-, and triphosphate binding experiments together with the RAMD data suggest that Trp<sup>21</sup> senses the nucleotide-bound state of the active site through its interaction with Arg<sup>140</sup>. Arg<sup>140</sup> probably remains in the apo state conformation when only monophosphate or diphosphate nucleotides bind to the active site (Fig. 10A). Because the C-terminal arm (including Arg<sup>140</sup>) is usually only visible in crystal structures that contain the triphosphate ligand, the apo state conformation of Arg<sup>140</sup> has never been reported before. However, the dUDP-complexed structure of the *M. tuberculosis* dUTPase is available for comparison for the position and mobility of Arg<sup>140</sup> in two different nucleotide-bound states (Fig. 11). By comparing the relative B-factors of Arg<sup>140</sup> within the same structure in Fig. 11 (*A* and *B*), it is clear that with a lack of the  $\gamma$ -phosphate, the mobility of the Arg residue is much higher. This phenomenon suggests that only a relatively static Arg<sup>140</sup> is able to change the fluorescence properties of Trp<sup>21</sup>, probably through cation- $\pi$  interaction, and thus yields a specific sensor for nucleoside triphosphate binding. It is interesting that modification of the electrostatic properties of the aromatic interacting partner (*i.e.* His to Trp change) perturbed the nucleotide affinities to the enzyme (Table 3). A possible explanation to this phenomenon may be that the Arg<sup>140</sup>—

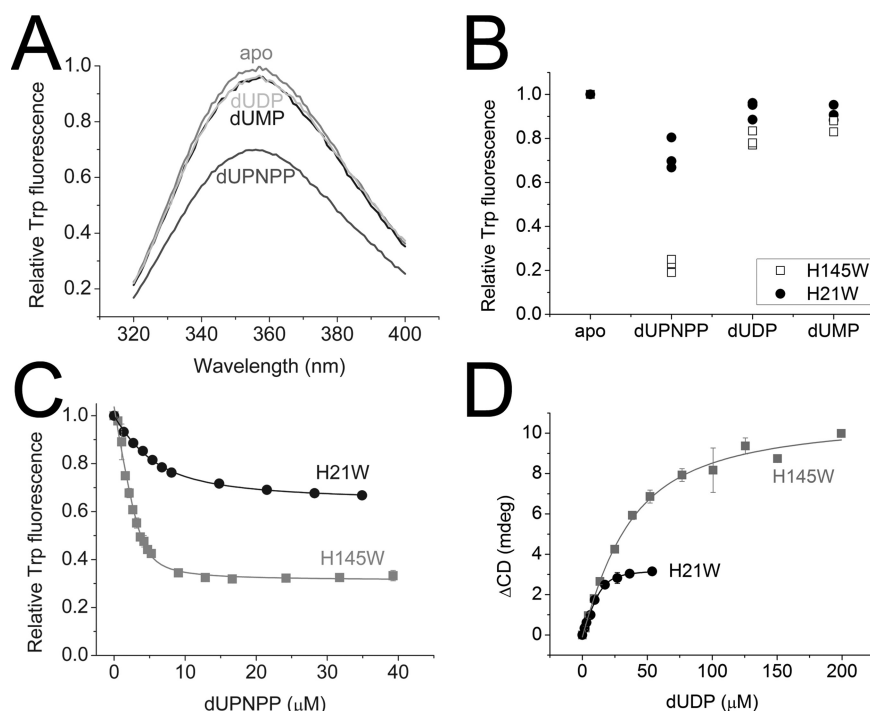


FIGURE 10. **Fluorescence and circular dichroism studies of ligand binding to the H145W and H21W mutants.** A, fluorescence spectra of the H21W mutant enzyme with and without nucleoside mono-, di-, and triphosphate ligands. B, fluorescence intensities of the H145W (49) and H21W mutant enzymes with saturating ligand concentrations. C, fluorescence titration of H145W and H21W with the dUPNPP substrate analogue; quadratic fit to the data yielded dissociation constants ( $K_{d,dUPNPP}$ ) shown in Table 3. D, circular dichroism titration of H145W and H21W with dUDP; quadratic fit to the data yielded dissociation constants ( $K_{d,dUDP}$ ) shown in Table 3.

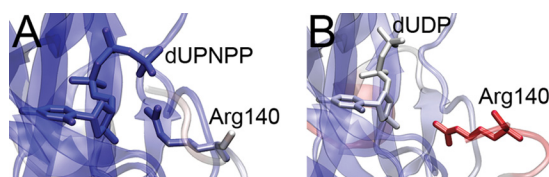


FIGURE 11. **Thermal mobility of the Arg<sup>140</sup> residue in various ligand bound complexes.** The enzyme is shown as thick transparent ribbon, whereas the ligand and Arg<sup>140</sup> are visualized as sticks. Coloring represents the relative crystallographic B factor for each atom (blue, less mobility; red, more mobility). A, the structure of *M. tuberculosis* dUTPase complexed with dUPNPP (PDB code 1SIX (10)). B, the structure of *M. tuberculosis* dUTPase complexed with dUDP (PDB code 1SLH (10)). Note that Arg<sup>140</sup> is in different conformation and that Arg<sup>140</sup> has much more mobility compared with the dUPNPP-complexed structure.

Trp<sup>21</sup> interaction is more stable than the Arg<sup>140</sup>–His<sup>21</sup> interaction in the WT. This in turn results in less frequent dislocation of the C-terminal arm (Fig. 7) and finally in the slower kinetics observed for dUTP binding (Table 3).

**Solvent Accessibility**—The solvent accessibility of the incorporated Trp<sup>21</sup> residue was measured by acrylamide quenching to obtain further dynamic information about the vicinity of the studied interaction. The acrylamide quenching of *N*-acetyl-L-tryptophanamide (NATA) was measured as reference and control for a rotationally free and maximally solvent-accessible Trp residue. The quenching constants ( $K_{SV}$ ) for the apo and the dUPNPP-bound enzymes were similar and significantly reduced compared with NATA (Fig. 12). The solvent accessibility of the active site Trp in the apo state and in the dUPNPP-bound complex are also shown for comparison (12). The comparative data indicate that the Trp<sup>21</sup> residue is buried similarly to the active site Trp. This suggests that part of the C-terminal

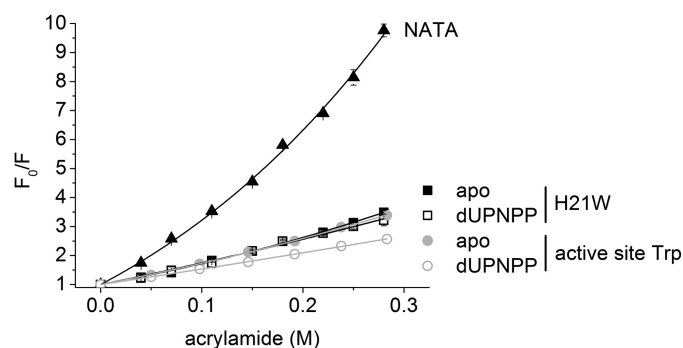


FIGURE 12. **Solvent accessibility of Trp<sup>21</sup> with and without ligand bound to the protein.** Acrylamide titration curves are shown. The modified Stern-Volmer equation was fitted to the data yielding quenching constants 18.8, 6.4, 7.1, 6.7, and 5.3 M<sup>-1</sup> for NATA, apo H21W, dUPNPP-bound H21W, apo active site Trp, and dUPNPP-bound active site Trp, respectively.

arm shielding Trp<sup>21</sup> from the solvent is associated to the protein core in equilibrium even in the apo enzyme. Consistently in all of the RAMD runs, we also observed that the C-terminal arm remains associated with the enzyme core following dUTP dissociation.

## Discussion

This study combined computational, biochemical, and biophysical methods to gain insights into the nucleotide binding of a nucleotide-hydrolyzing enzyme at exceptionally high time and structural resolution. The RAMD method provided the high time and structural resolution, whereas the numerous experimental data served to validate the results of the computational simulation. In terms of mechanistic detail, the RAMD runs can be regarded as fast transient kinetics experiments on a



single molecule level. It appears that the assembly of the phenomena observed in single RAMD runs agrees well with the ensemble solution kinetics results presented earlier. The RAMD models reveal how the substrate can leave/enter the active site without completely opening the C-terminal arm. A previously hypothesized mechanism like a “hinge door” in which the C-terminal arm completely opens up at the hinge of a conserved Pro (51) was not observed in the RAMD simulations. Instead, we observed the nucleotide shuttling between the active site and the solvent through small openings of the C-terminal arm. The arm, fixed at both ends to the enzyme core via secondary interactions, moves only by sliding away close to the enzyme surface or by opening partially and locally. These movements involving 10–15 residues are small compared to the conformational changes observed for other nucleotide binding enzymes (4, 5, 52). In DNA helicases and polymerases, substrate binding involves displacement of whole domains (1–3, 6). It should be mentioned that the RAMD method may not be capable of modeling large loop motions because relevant reports are missing. However, our computational simulations and spectroscopic results together unequivocally support the finding that small loop movements allow the shuttling of the nucleotides between the binding pocket and the solvent in dUTPase, whereas larger scale movements may not be excluded.

There may be an apparent contradiction between the C-terminal arm not being visible in the crystal structures and the RAMD simulations showing only small amplitude movements of the C-terminal arm. These phenomena, however, are complementary. The electron density maps represent the average conformation of all atoms in a protein crystal. The inability to localize an entity may be due to movements on a small amplitude scale just exceeding the atomic distance. Molecular dynamics simulations, on the other hand, investigate single molecules rather than a population average and commonly reveal small amplitude movements. The example of dUTPase demonstrates that the comparison of crystal structures in various nucleotide-bound states alone is not fully informative of the nucleotide binding mechanism.

This study yielded novel insights regarding the dynamics and other properties of the interaction between dUTP and  $\text{Mg}^{2+}$  as well. The RAMD method offered a unique opportunity to observe that this interaction is maintained during the whole ligand binding/unbinding process, although the octahedral coordination between  $\text{Mg}^{2+}$  and dUTP became distorted in some of the pathways.

As proof of principle, we chose the His<sup>21</sup> residue *de novo* predicted by the RAMD simulations to be involved in substrate dissociation to validate our data. It turned out that the replacement of this residue with a Trp yielded a sensitive fluorescence reporter specific to triphosphate nucleotide binding. As such, Trp<sup>21</sup> reported the hydrolysis reaction similarly to the active site nucleotide sensor, Trp<sup>145</sup>. Using the combination of structural and optical spectroscopic methods, we proposed a possible molecular mechanism for nucleotide sensing by Trp<sup>21</sup> relatively far from the active site. This phenomenon also shines light onto the possibility to exploit this specific interaction in target-based drug design against actinobacterial pathogens.

## Experimental Procedures

**System Preparation for Molecular Dynamics Simulation**—The initial structure for the simulations was the crystal structure of the *M. tuberculosis* dUTPase complexed with dUPNPP (PDB code 2PY4 (33)). The original dUPNPP ligand in the crystal structure was manually modified to dUTP. The protonation states of the titratable groups were determined by means of the ProPka algorithm (53, 54) at pH 7.4, and the optimization of hydrogen bonding interactions was performed using the PDB2PQR program package (55). The structure obtained was solvated using the TIP3P water model (56), and a minimum distance of 14 Å was used between any atom of the protein and the wall of the periodic box. The number of  $\text{Na}^+$  cations and  $\text{Cl}^-$  anions was 49 and 34, respectively, to neutralize the system and mimic the physiological ionic strength (0.15 M NaCl). For description of the protein and dUTP, the CHARMM27 parameters (57) including the CMAP correction term for proteins (58) were applied, whereas the ions were described by the parameters of Beglov and Roux (59).

**Molecular Dynamics Simulations**—Molecular dynamics simulations were performed with the NAMD2.7 software (60) applying the following protocol: (i) 1600 steps minimization with restrained protein atoms using a 10 kcal mol<sup>−1</sup> Å<sup>−2</sup> force constant; (ii) 3200 steps minimization; (iii) 32-ps NVT dynamics, where number of atoms (N), volume (V), and temperature (T) are fixed ( $T = 310$  K, Langevin dynamics (61)) with restrained protein atoms using a 10 kcal mol<sup>−1</sup> Å<sup>−2</sup> force constant; and (iv) NPT dynamics, where number of atoms (N), pressure (P), and temperature (T) are fixed ( $p = 1$  atm,  $T = 310$  K) with the Noosé-Hoover Langevin piston method (61, 62). The time step was set to 1 fs, a cutoff value of 10 Å was applied (using a smoothing function from 8 Å), and the long range electrostatic interactions were calculated with the Particle Mesh Ewald (PME) method (63). Two independent, 2-ns-long simulations with different initial velocities were conducted to relax the system, and the structures of the last frames were used in the subsequent RAMD simulations. During the 300-ps-long RAMD simulations, the acceleration was set to 0.066 kcal mol<sup>−1</sup> Å<sup>−1</sup> (atomic mass unit)<sup>−1</sup>, and the successful exit event was accepted if the distance between the center of mass of protein and that of dUTP was larger than 50 Å. Every 80 fs, new orientation was generated if the distance traveled by the ligand was less than 0.1 Å, and the trajectory was saved every 80 fs. No restraints were applied when conducting the RAMD simulations. From both starting structures and every binding cavity, 12 RAMD simulations were started resulting in 72 calculations. Once the ligand escapes into the solvent, the dissociation pathway becomes smooth because of the constant force acting on the substrate. This linearity of the ligand trajectories within the bulk solvent is irrelevant for the ligand finding the possible paths out of the active site.

**Analysis of the Trajectories**—Analysis of the trajectories was performed with the Visual Molecular Dynamics (64) package, which was used to generate Figs. 1–4, 7, 8, and 11 and [supplemental Movies S1–S5](#).

**Reagents**—Molecular biology products were from New England Biolabs and Fermentas, electrophoresis and chromatogra-

phy reagents were from Bio-Rad and Qiagen. Phenol red was from Merck, dUDP and dUPNPP was from Jena Bioscience, and dUTP and other chemicals were from Sigma-Aldrich.

**Mutagenesis**—To generate the *M. tuberculosis* H21W mutant dUTPase, site-directed mutagenesis was performed by Stratagene's QuikChange method and was verified by sequencing. The mutagenic forward and reverse primers were 5'-GCCCAGCCGCGCTTGGGACGGCGACGCCG-GCG-3' and 5'-CGCCGGCGTCCCGTCCCAAGCGCGG-CTGGGC-3'.

**Cloning, Protein Expression, and Purification**—were performed as described previously in Ref. 33. Recombinant dUTPase with an N-terminal His<sub>6</sub> tag was transformed into *Escherichia coli* strain Rosetta(DE3)pLysS, which was used for protein expression. The final supernatant after cell extraction was loaded on a nickel-nitrilotriacetic acid column (Novagen) and purified according to the Novagen protocol. Because wild type lacks a useful tryptophan to monitor ligand binding, we have used the H145W mutant for kinetic studies. This tryptophan substitution in the active site has been previously shown to not affect catalytic activity (33). Protein concentration was measured using the Bradford method (Bio-Rad protein assay) and is given in subunits. Protein was dialyzed against buffer pH 7.5, containing 20 mM HEPES, 100 mM NaCl, 2 mM MgCl<sub>2</sub>, and 1 mM DTT, and measurements were carried out in this buffer if not stated otherwise.

**Crystallization**—The H21W mutant was crystallized as described for the WT enzyme using the hanging drop diffusion method (33). 250  $\mu$ M dUTPase and 1.25 mM dUPNPP were mixed with the reservoir solution containing 50 mM Tris-HCl, pH 7.5, 10 mM MgCl<sub>2</sub>, 1.20–1.75 M ammonium sulfate, and 10% glycerol in a 1:1 ratio.

**Data Collection and Structure Determination**—High resolution complete crystallographic data set from a single flash frozen crystal was collected at Eötvös University using RIGAKU RU-H2R rotating anode home source at  $\lambda = 1.5418$  Å on 100 K temperature. Reflection data were recorded on RIGAKU R-Axis IV++ image plate detector.

Data reduction was performed using iMosflm and Scala programs and the CCP4 program suite (65). The structure of the H21W mutant in complex with dUPNPP and Mg<sup>2+</sup> was determined by molecular replacement using MolRep, where the model was the WT dUTPase structure (PDB code 2PY4 (33)).  $R_{\text{merge}} = \sum(|I_i - \langle I \rangle|) / \sum(\langle I \rangle)$ , where the sum is calculated over all observations of a measured reflection ( $I_i$ ), and  $\langle I \rangle$  is the mean intensity of all the measured observations ( $I_i$ ).

Manual model building was carried out running the WinCoot program (66). Refmac5 software from CCP4 program package (65) was used for high resolution refinement.  $R_{\text{free}}$  values were computed from cross-validation throughout the refinement, using 5% random subset of the data set. Ramachandran statistics were as follows: 99.3% favored, 0.7% additionally allowed, and 0% generously allowed. The coordinates and structure factor data have been deposited in the Protein Data Bank under PDB code 4GCY.

**Steady-state Colorimetric dUTPase Assay**—Steady-state colorimetric dUTPase assay was performed as described in Ref. 35. Phenol red indicator assay was used to detect protons released

in the dUTPase reaction. 0.1  $\mu$ M protein was used in a buffer containing 1 mM HEPES, pH 7.5, 100 mM KCl, 40  $\mu$ M phenol red, and 5 mM MgCl<sub>2</sub>. A Specord 200 (Analytic, Jena, Germany) spectrophotometer and 10-mm-path length cuvettes were used at 20 °C, and absorbance was recorded at 559 nm. Initial velocity was determined from the first 10% of the progress curve.

**Stopped Flow Experiments**—Measurements were done using an SX-20 (Applied Photophysics) stopped flow apparatus as described in Refs. 12 and 35. Trp fluorescence was excited at 297 nm, and emission was selected with a 320-nm long pass filter. Time courses were recorded upon mixing sub- and superstoichiometric concentrations of dUTP with 1 or 3  $\mu$ M enzyme at 20 °C (post-mix concentrations). Single turnover curves could be fitted with three exponentials (12). The two fast phases represent ligand binding, whereas the third, fluorescence recovery phase represents the hydrolysis-limited product release event and yields the single turnover rate constant (12). The fluorescence decrease of the time courses resulted from mixing excess dUTP over active sites and was fitted with double exponential function. Each time course shown is the mean of five measurements recorded sequentially in the same experiment. The  $k_{\text{obs}}$  versus dUTP concentration plots show the mean and standard error of three independent measurements. Time courses were analyzed using the curve fitting software provided with the stopped flow apparatus or by Origin 7.5. (OriginLab Corp., Northampton, MA).

**Determination of the Enzyme-Ligand Dissociation Constants**—Determination of the enzyme-ligand dissociation constants was done by fluorescence intensity titrations and circular dichroism intensity titrations. Fluorescence intensity titrations were recorded at 20 °C on a Jobin Yvon Spex Fluoromax-3 spectrofluorometer with excitation at 295 nm (slit, 1 nm), emission at 347 nm (slit 5 nm) using proteins at 4  $\mu$ M concentration as described in Ref. 49. CD spectra were recorded at 20 °C on a JASCO 720 spectropolarimeter using a 10-mm-path length cuvette. Protein concentration was 50  $\mu$ M in a buffer containing 20 mM HEPES, pH 7.5, 50 mM NaCl, and 2 mM MgCl<sub>2</sub>. A spectrum between 250 and 290 nm was recorded at each nucleotide concentration as described in Ref. 35. Differential curves were obtained by subtracting the signal of the ligand alone from that of the corresponding complex. Differential ellipticity at 269 nm was plotted against the ligand concentration to obtain the binding curves.

In both types of measurement, protein solution was titrated with dUPNPP or dUDP using small volumes from a concentrated stock solution. The following equation describing 1:1 stoichiometry for the dissociation equilibrium was fitted to the titration data,

$$y = s + \frac{A[(c + x + K) - \sqrt{(c + x + K)^2 - 4cx}]}{2c}$$

(Eq. 1)

where  $x$  is the nucleotide concentration,  $y$  is the fluorescence or circular dichroism intensity,  $s = y$  at  $x = 0$ ,  $A$  is the amplitude of the fluorescence or circular dichroism intensity change,  $c$  is the enzyme concentration, and  $K$  is the dissociation constant ( $K_d$ ).

**Acrylamide Quenching**—Acrylamide quenching was carried out by the addition of small volumes of a 5 M acrylamide solution to the enzyme, enzyme-dUTPase, or NATA solutions as described in Ref. 12. Raw data were corrected for the fluorescence arising from the acrylamide solution itself.  $F_0/F$  versus  $[Q]$  curves were analyzed using a modified Stern-Volmer equation,

$$F_0/F = 1 + K_{SV}[Q]e^{V[Q]} \quad (\text{Eq. 2})$$

where  $F_0$  is the unquenched,  $F$  is the quenched fluorescence,  $[Q]$  is the quencher,  $K_{SV}$  is the dynamic (bimolecular) quenching constant, and  $V$  is the static (sphere of action) component of quenching.

**Author Contributions**—A. L. and B. J. conceived the idea for the project and carried out the simulations. A. L. conducted the *in vitro* experiments under J. T.'s supervision. I. L. and Á. Á. B. carried out structure determination. A. L., J. T., and B. J. analyzed the results. A. L., J. T., B. J., B. V., and B. G. V. wrote the paper.

**Acknowledgments**—We thank M. Lábadi for technical support at the High Performance Computing (HPC) Centre of the University of Szeged, Veronika Harmat for crystallography help, and Judit E. Szabó for useful comments on the manuscript.

## References

- Lee, J. Y., and Yang, W. (2006) UvrD helicase unwinds DNA one base pair at a time by a two-part power stroke. *Cell* **127**, 1349–1360
- Gai, D., Zhao, R., Li, D., Finkelstein, C. V., and Chen, X. S. (2004) Mechanisms of conformational change for a replicative hexameric helicase of SV40 large tumor antigen. *Cell* **119**, 47–60
- Velankar, S. S., Soultanas, P., Dillingham, M. S., Subramanya, H. S., and Wigley, D. B. (1999) Crystal structures of complexes of PcrA DNA helicase with a DNA substrate indicate an inchworm mechanism. *Cell* **97**, 75–84
- Sablin, E. P., and Fletterick, R. J. (2001) Nucleotide switches in molecular motors: structural analysis of kinesins and myosins. *Curr. Opin. Struct. Biol.* **11**, 716–724
- Shuman, S., and Lima, C. D. (2004) The polynucleotide ligase and RNA capping enzyme superfamily of covalent nucleotidyltransferases. *Curr. Opin. Struct. Biol.* **14**, 757–764
- Santoso, Y., Joyce, C. M., Potapova, O., Le Reste, L., Hohlbein, J., Torella, J. P., Grindley, N. D., and Kapanidis, A. N. (2010) Conformational transitions in DNA polymerase I revealed by single-molecule FRET. *Proc. Natl. Acad. Sci. U.S.A.* **107**, 715–720
- Fiser, A., and Vértessy, B. G. (2000) Altered subunit communication in subfamilies of trimeric dUTPases. *Biochem. Biophys. Res. Commun.* **279**, 534–542
- Vértessy, B. G., and Tóth, J. (2009) Keeping uracil out of DNA: physiological role, structure and catalytic mechanism of dUTPases. *Acc. Chem. Res.* **42**, 97–106
- Mol, C. D., Harris, J. M., McIntosh, E. M., and Tainer, J. A. (1996) Human dUTP pyrophosphatase: uracil recognition by a  $\beta$  hairpin and active sites formed by three separate subunits. *Structure* **4**, 1077–1092
- Chan, S., Segelke, B., Lakin, T., Krupka, H., Cho, U. S., Kim, M. Y., So, M., Kim, C. Y., Naranjo, C. M., Rogers, Y. C., Park, M. S., Waldo, G. S., Pashkov, I., Cascio, D., Perry, J. L., et al. (2004) Crystal structure of the *Mycobacterium tuberculosis* dUTPase: insights into the catalytic mechanism. *J. Mol. Biol.* **341**, 503–517
- Vértessy, B. G., Larsson, G., Persson, T., Bergman, A. C., Persson, R., and Nyman, P. O. (1998) The complete triphosphate moiety of non-hydrolyzable substrate analogues is required for a conformational shift of the flexible C-terminus in *E. coli* dUTP pyrophosphatase. *FEBS Lett.* **421**, 83–88
- Tóth, J., Varga, B., Kovács, M., Málnási-Csizmadia, A., and Vértessy, B. G. (2007) Kinetic mechanism of human dUTPase, an essential nucleotide pyrophosphatase enzyme. *J. Biol. Chem.* **282**, 33572–33582
- Shan, Y., Kim, E. T., Eastwood, M. P., Dror, R. O., Seeliger, M. A., and Shaw, D. E. (2011) How does a drug molecule find its target binding site? *J. Am. Chem. Soc.* **133**, 9181–9183
- Dror, R. O., Pan, A. C., Arlow, D. H., Borhani, D. W., Maragakis, P., Shan, Y., Xu, H., and Shaw, D. E. (2011) Pathway and mechanism of drug binding to G-protein-coupled receptors. *Proc. Natl. Acad. Sci. U.S.A.* **108**, 13118–13123
- Dror, R. O., Green, H. F., Valant, C., Borhani, D. W., Valcourt, J. R., Pan, A. C., Arlow, D. H., Canals, M., Lane, J. R., Rahmani, R., Baell, J. B., Sexton, P. M., Christopoulos, A., and Shaw, D. E. (2013) Structural basis for modulation of a G-protein-coupled receptor by allosteric drugs. *Nature* **503**, 295–299
- Thomas, T., Fang, Y., Yuriev, E., and Chalmers, D. K. (2016) Ligand binding pathways of clozapine and haloperidol in the dopamine D<sub>2</sub> and D<sub>3</sub> receptors. *J. Chem. Inf. Model.* **56**, 308–321
- Gao, M., Craig, D., Vogel, V., and Schulten, K. (2002) Identifying unfolding intermediates of FN-III(10) by steered molecular dynamics. *J. Mol. Biol.* **323**, 939–950
- Lüdemann, S. K., Lounnas, V., and Wade, R. C. (2000) How do substrates enter and products exit the buried active site of cytochrome P450cam?: 2. Steered molecular dynamics and adiabatic mapping of substrate pathways. *J. Mol. Biol.* **303**, 813–830
- Lüdemann, S. K., Lounnas, V., and Wade, R. C. (2000) How do substrates enter and products exit the buried active site of cytochrome P450cam?: 1. Random expulsion molecular dynamics investigation of ligand access channels and mechanisms. *J. Mol. Biol.* **303**, 797–811
- Gervasio, F. L., Parrinello, M., Ceccarelli, M., and Klein, M. L. (2006) Exploring the gating mechanism in the CIC chloride channel via metadynamics. *J. Mol. Biol.* **361**, 390–398
- Grazioso, G., Limongelli, V., Branduardi, D., Novellino, E., De Micheli, C., Cavalli, A., and Parrinello, M. (2012) Investigating the mechanism of substrate uptake and release in the glutamate transporter homologue Glt(Ph) through metadynamics simulations. *J. Am. Chem. Soc.* **134**, 453–463
- Wang, T., and Duan, Y. (2007) Chromophore channeling in the G-protein coupled receptor rhodopsin. *J. Am. Chem. Soc.* **129**, 6970–6971
- Klvana, M., Pavlova, M., Koudelakova, T., Chaloupkova, R., Dvorak, P., Prokop, Z., Stsiapanava, A., Kutý, M., Kuta-Smatanova, I., Dohnalek, J., Kulhanek, P., Wade, R. C., and Damborsky, J. (2009) Pathways and mechanisms for product release in the engineered haloalkane dehalogenases explored using classical and random acceleration molecular dynamics simulations. *J. Mol. Biol.* **392**, 1339–1356
- Kalyanamoorthy, S., and Chen, Y.-P. (2012) Exploring inhibitor release pathways in histone deacetylases using random acceleration molecular dynamics simulations. *J. Chem. Inf. Model.* **52**, 589–603
- Pietra, F. (2013) On the pathways of biologically relevant diatomic gases through proteins: dioxygen and heme oxygenase from the perspective of molecular dynamics. *Chem. Biodivers.* **10**, 556–568
- Zhuang, S., Bao, L., Linhananta, A., and Liu, W. (2013) Molecular modeling revealed that ligand dissociation from thyroid hormone receptors is affected by receptor heterodimerization. *J. Mol. Graph. Model.* **44**, 155–160
- Zhang, J., Li, D., Sun, T., Liang, L., and Wang, Q. (2015) Interaction of P-glycoprotein with anti-tumor drugs: the site, gate and pathway. *Soft Matter* **11**, 6633–6641
- Niu, Y., Li, S., Pan, D., Liu, H., and Yao, X. (2016) Computational study on the unbinding pathways of B-Raf inhibitors and its implication for the difference of residence time: insight from random acceleration and steered molecular dynamics simulations. *Phys. Chem. Chem. Phys.* **18**, 5622–5629
- Prasad, G. S., Stura, E. A., Elder, J. H., and Stout, C. D. (2000) Structures of feline immunodeficiency virus dUTP pyrophosphatase and its nucleotide complexes in three crystal forms. *Acta Crystallogr. D Biol. Crystallogr.* **56**, 1100–1109



30. González, A., Larsson, G., Persson, R., and Cedergren-Zeppeauer, E. (2001) Atomic resolution structure of *Escherichia coli* dUTPase determined ab initio. *Acta Crystallogr. D Biol. Crystallogr.* **57**, 767–774
31. Barabás, O., Pongrácz, V., Kovári, J., Wilmanns, M., and Vértessy, B. G. (2004) Structural insights into the catalytic mechanism of phosphate ester hydrolysis by dUTPase. *J. Biol. Chem.* **279**, 42907–42915
32. Tarbouriech, N., Buisson, M., Seigneurin, J. M., Cusack, S., and Burmeister, W. P. (2005) The monomeric dUTPase from Epstein-Barr virus mimics trimeric dUTPases. *Structure* **13**, 1299–1310
33. Varga, B., Barabás, O., Takács, E., Nagy, N., Nagy, P., and Vértessy, B. G. (2008) Active site of mycobacterial dUTPase: structural characteristics and a built-in sensor. *Biochem. Biophys. Res. Commun.* **373**, 8–13
34. Freeman, L., Buisson, M., Tarbouriech, N., Van der Heyden, A., Labbé, P., and Burmeister, W. P. (2009) The flexible motif V of Epstein-Barr virus deoxyuridine 5'-triphosphate pyrophosphatase is essential for catalysis. *J. Biol. Chem.* **284**, 25280–25289
35. Pecs, I., Leveles, I., Harmat, V., Vértessy, B. G., and Toth, J. (2010) Aromatic stacking between nucleobase and enzyme promotes phosphate ester hydrolysis in dUTPase. *Nucleic Acids Res.* **38**, 7179–7186
36. Larsson, G., Nyman, P. O., and Kvassman, J. O. (1996) Kinetic characterization of dUTPase from *Escherichia coli*. *J. Biol. Chem.* **271**, 24010–24016
37. Nord, J., Kiefer, M., Adolph, H. W., Zeppeauer, M. M., and Nyman, P. O. (2000) Transient kinetics of ligand binding and role of the C-terminus in the dUTPase from equine infectious anemia virus. *FEBS Lett.* **472**, 312–316
38. Tormo-Más, M. A., Mir, I., Shrestha, A., Tallent, S. M., Campoy, S., Lasa, I., Barbé, J., Novick, R. P., Christie, G. E., and Penadés, J. R. (2010) Moonlighting bacteriophage proteins derepress staphylococcal pathogenicity islands. *Nature* **465**, 779–782
39. Szabó, J. E., Németh, V., Papp-Kádár, V., Nyíri, K., Leveles, I., Bendes, A. Á., Zagyva, I., Róna, G., Pálkás, H. L., Besztercei, B., Ozohanic, O., Vékey, K., Liliom, K., Tóth, J., and Vértessy, B. G. (2014) Highly potent dUTPase inhibition by a bacterial repressor protein reveals a novel mechanism for gene expression control. *Nucleic Acids Res.* **42**, 11912–11920
40. Hill, R. L., and Dokland, T. (2016) The type 2 dUTPase of bacteriophage  $\phi$ NM1 initiates mobilization of *Staphylococcus aureus* bovine pathogenicity island 1. *J. Mol. Biol.* **428**, 142–152
41. Pécsi, I., Szabó, J. E., Adams, S. D., Simon, I., Sellers, J. R., Vértessy, B. G., and Tóth, J. (2011) Nucleotide pyrophosphatase employs a P-loop-like motif to enhance catalytic power and NDP/NTP discrimination. *Proc. Natl. Acad. Sci. U.S.A.* **108**, 14437–14442
42. Pecs, I., Hirmondo, R., Brown, A. C., Lopata, A., Parish, T., Vértessy, B. G., and Tóth, J. (2012) The dUTPase enzyme is essential in *Mycobacterium smegmatis*. *PLoS One* **7**, e37461
43. Muha, V., Horváth, A., Békési, A., Pukáncsik, M., Hodoscsek, B., Merényi, G., Róna, G., Batki, J., Kiss, I., Jankovics, F., Vilmos, P., Erdélyi, M., and Vértessy, B. G. (2012) Uracil-containing DNA in *Drosophila*: stability, stage-specific accumulation, and developmental involvement. *PLoS Genet.* **8**, e1002738
44. Vértessy, B. G. (1997) Flexible glycine rich motif of *Escherichia coli* deoxyuridine triphosphate nucleotidohydrolase is important for functional but not for structural integrity of the enzyme. *Proteins* **28**, 568–579
45. Németh-Pongrácz, V., Barabás, O., Fuxreiter, M., Simon, I., Pichová, I., Rumlová, M., Zábranská, H., Svergun, D., Petoukhov, M., Harmat, V., Klement, E., Hunyadi-Gulyás, E., Medzihradsky, K. F., Kónya, E., and Vértessy, B. G. (2007) Flexible segments modulate co-folding of dUTPase and nucleocapsid proteins. *Nucleic Acids Res.* **35**, 495–505
46. García-Nafria, J., Burchell, L., Takezawa, M., Rzechorzek, N. J., Fogg, M. J., and Wilson, K. S. (2010) The structure of the genomic *Bacillus subtilis* dUTPase: novel features in the Phe-lid. *Acta Crystallogr. D Biol. Crystallogr.* **66**, 953–961
47. Cojocar, V., Winn, P. J., and Wade, R. C. (2012) Multiple, ligand-dependent routes from the active site of cytochrome P450 2C9. *Curr. Drug Metab.* **13**, 143–154
48. Nord, J., Nyman, P., Larsson, G., and Drakenberg, T. (2001) The C-terminus of dUTPase: observation on flexibility using NMR. *FEBS Lett.* **492**, 228–232
49. Takács, E., Nagy, G., Leveles, I., Harmat, V., Lopata, A., Tóth, J., and Vértessy, B. G. (2010) Direct contacts between conserved motifs of different subunits provide major contribution to active site organization in human and mycobacterial dUTPases. *FEBS Lett.* **584**, 3047–3054
50. Shao, H., Robek, M. D., Threadgill, D. S., Mankowski, L. S., Cameron, C. E., Fuller, F. J., and Payne, S. L. (1997) Characterization and mutational studies of equine infectious anemia virus dUTPase. *Biochim. Biophys. Acta* **1339**, 181–191
51. Takács, E., Barabás, O., Petoukhov, M. V., Svergun, D. I., and Vértessy, B. G. (2009) Molecular shape and prominent role of beta-strand swapping in organization of dUTPase oligomers. *FEBS Lett.* **583**, 865–871
52. Yang, S.-W., Ting, H.-C., Lo, Y.-T., Wu, T.-Y., Huang, H.-W., Yang, C.-J., Chan, J.-F. R., Chuang, M.-C., and Hsu, Y.-H. (2016) Guanine nucleotide induced conformational change of Cdc42 revealed by hydrogen/deuterium exchange mass spectrometry. *Biochim. Biophys. Acta* **1864**, 42–51
53. Li, H., Robertson, A. D., and Jensen, J. H. (2005) Very fast empirical prediction and rationalization of protein pKa values. *Proteins* **61**, 704–721
54. Bas, D. C., Rogers, D. M., and Jensen, J. H. (2008) Very fast prediction and rationalization of pKa values for protein-ligand complexes. *Proteins* **73**, 765–783
55. Dolinsky, T. J., Nielsen, J. E., McCammon, J. A., and Baker, N. A. (2004) PDB2PQR: an automated pipeline for the setup of Poisson-Boltzmann electrostatics calculations. *Nucleic Acids Res.* **32**, W665–7
56. Jorgensen, W. L., Chandrasekhar, J., Madura, J. D., Impey, R. W., and Klein, M. L. (1983) Comparison of simple potential functions for simulating liquid water. *J. Chem. Phys.* **79**, 926–935
57. MacKerell, A. D., Bashford, D., Bellott, M., Dunbrack, R. L., Evanseck, J. D., Field, M. J., Fischer, S., Gao, J., Guo, H., Ha, S., Joseph-McCarthy, D., Kuchnir, L., Kuczera, K., Lau, F. T., Mattos, C., et al. (1998) All-atom empirical potential for molecular modeling and dynamics studies of proteins. *J. Phys. Chem. B* **102**, 3586–3616
58. Mackerell, A. D., Jr., Feig, M., and Brooks, C. L., 3rd (2004) Extending the treatment of backbone energetics in protein force fields: Limitations of gas-phase quantum mechanics in reproducing protein conformational distributions in molecular dynamics simulations. *J. Comput. Chem.* **25**, 1400–1415
59. Beglov, D., and Roux, B. (1994) Finite representation of an infinite bulk system: solvent boundary potential for computer-simulations. *J. Chem. Phys.* **100**, 9050–9063
60. Phillips, J. C., Braun, R., Wang, W., Gumbart, J., Tajkhorshid, E., Villa, E., Chipot, C., Skeel, R. D., Kalé, L., and Schulten, K. (2005) Scalable molecular dynamics with NAMD. *J. Comput. Chem.* **26**, 1781–1802
61. Feller, S. E., Zhang, Y. H., Pastor, R. W., and Brooks, B. R. (1995) Constant-pressure molecular-dynamics simulation: the Langevin piston method. *J. Chem. Phys.* **103**, 4613–4621
62. Martyna, G. J., Tobias, D. J., and Klein, M. L. (1994) Constant-pressure molecular-dynamics algorithms. *J. Chem. Phys.* **101**, 4177–4189
63. Darden, T., York, D., and Pedersen, L. (1993) Particle mesh Ewald: an N. Log(N) method for Ewald sums in large systems. *J. Chem. Phys.* **98**, 10089–10092
64. Humphrey, W., Dalke, A., and Schulten, K. (1996) VMD: Visual molecular dynamics. *J. Mol. Graph.* **14**, 33–38
65. Winn, M. D., Ballard, C. C., Cowtan, K. D., Dodson, E. J., Emsley, P., Evans, P. R., Keegan, R. M., Krissinel, E. B., Leslie, A. G., McCoy, A., McNicholas, S. J., Murshudov, G. N., Pannu, N. S., Potterton, E. A., Powell, H. R., et al. (2011) Overview of the CCP4 suite and current developments. *Acta Crystallogr. D Biol. Crystallogr.* **67**, 235–242
66. Emsley, P., and Cowtan, K. (2004) Coot: model-building tools for molecular graphics. *Acta Crystallogr. D Biol. Crystallogr.* **60**, 2126–2132